Magnetic and Orbital Ordering in the Spinel MnV_2O_4

V. O. Garlea,[1,*] R. Jin,[2] D. Mandrus,[2] B. Roessli,[3] Q. Huang,[4] M. Miller,[5] A. J. Schultz,[5] and S. E. Nagler[1]

[1]*Neutron Scattering Science Division, Oak Ridge National Laboratory, Oak Ridge, Tennessee 37831, USA*
[2]*Materials Science and Technology Division, Oak Ridge National Laboratory, Oak Ridge, Tennessee 37831, USA*
[3]*Laboratory for Neutron Scattering ETHZ & Paul Scherrer Institute, CH-5232 Villigen PSI, Switzerland*
[4]*NIST Center for Neutron Research, Gaithersburg, Maryland 20899, USA*
[5]*IPNS Division, Argonne National Laboratory, Argonne, Illinois 60439, USA*

(Received 13 November 2007; published 14 February 2008)

Neutron inelastic scattering and diffraction techniques have been used to study the MnV_2O_4 spinel system. Our measurements show the existence of two transitions to long-range ordered ferrimagnetic states, the first collinear and the second noncollinear. The lower temperature transition, characterized by development of antiferromagnetic components in the basal plane, is accompanied by a tetragonal distortion and the appearance of a gap in the magnetic excitation spectrum. The low-temperature noncollinear magnetic structure has been definitively resolved. Taken together, the crystal and magnetic structures indicate a staggered ordering of the V d orbitals. The anisotropy gap is a consequence of unquenched V orbital angular momentum.

DOI: 10.1103/PhysRevLett.100.066404 PACS numbers: 71.70.Ej, 75.25.+z, 75.50.Gg, 78.70.Nx

Understanding the consequences of orbital degeneracy, and the interplay of spin, orbital, and lattice degrees of freedom, has emerged as a forefront area of condensed matter physics. One of the most investigated prototypical systems in which these effects are important is the vanadium oxide spinel, with formula AV_2O_4. There has been much experimental and theoretical effort to understand the properties of AV_2O_4 [1–9], where A is a nonmagnetic species such as Mg [1], Zn [2], or Cd [3]. As is well known, the V^{3+} ($3d^2$) ion sits in a position of local octahedral symmetry and therefore has a threefold degenerate orbital ground state. Furthermore, the V^{3+} ions occupy the vertices of a tetrahedron and their mutual antiferromagnetic superexchange interactions are topologically frustrated. A common feature found in these materials is a sequence of two phase transitions [1–3]. The higher temperature transition is a structural distortion involving a compression of the VO_6 octahedra and a consequent partial lifting of the orbital degeneracy. The orbital ordering is accompanied, at lower temperature, by an antiferromagnetic ordering. Various models [4–9] have been proposed to explain this behavior. However, up to date, there is not yet a full consensus on the precise nature of the orbital ordering.

Replacing the atom at the A site by a magnetic species changes the physics, leading to different and very interesting behavior. Recent attention has turned to MnV_2O_4 [10–13], where the A site ion, Mn^{2+}, is in a $3d^5$ high spin configuration $S = 5/2$ with quenched orbital angular momentum. MnV_2O_4 exhibits at about 56 K a transition from a paramagnetic into a collinear ferrimagnetic phase. Around 53 K there is a second transition to a tetragonal structure, with the spin structure becoming noncollinear [10]. Recently, it was found that the cubic to tetragonal transition could be induced by a modest magnetic field of a few Tesla [11,12]. In addition, it has been suggested that the system also exhibits a reentrant spin glass behavior [13]. In this Letter we report the results of neutron scattering measurements on both powder and single-crystal samples of MnV_2O_4. Our measurements confirm the existence of two phase transitions and allow for a definitive determination of the low-temperature noncollinear ferrimagnetic structure. Inelastic neutron scattering shows that the cubic to tetragonal transition is associated with the opening of a gap in the magnetic excitation spectrum. These observations put tight constraints on theoretical models for MnV_2O_4.

The powder sample used in this study was prepared by solid-state reaction from stoichiometric mixture of MnO and V_2O_3. MnV_2O_4 single crystals were grown using the floating-zone technique. All samples were characterized by x-ray diffraction and magnetization measurements. The temperature dependence of the low field (0.1 kOe) magnetization of a MnV_2O_4 single-crystal under zero-field-cooling (ZFC) and field-cooling (FC) conditions is shown in Fig. 1(a). Qualitatively, the magnetization curves look similar to those reported previously [12,13]. Upon decreasing temperature, the FC magnetization goes through a maximum and shows a sharp decrease before it starts to increase again. As visible in Fig. 1(a), the rapid decrease in magnetization, near 50 K, marks the point where the FC and ZFC curves begin to diverge.

To monitor the changes in the crystal and magnetic structures across these transitions, several neutron scattering experiments were performed. Time-of-flight diffraction measurements were carried out using the single-crystal diffractometer (SCD) at the IPNS, on a 0.2 g single-crystal specimen. High-resolution neutron powder diffraction data were collected on the BT1 diffractometer, at the NCNR, using the wavelength 1.54 Å. Additional elastic and inelastic measurements were conducted using

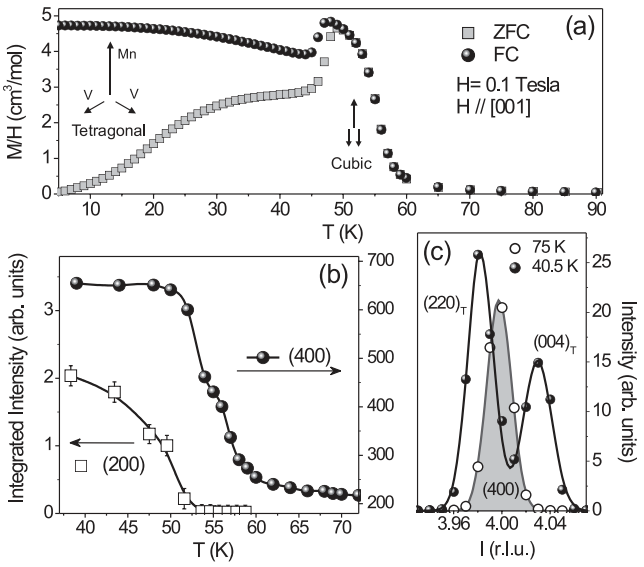

FIG. 1. (a) The zero-field-cooling (ZFC) and the field-cooling (FC) temperature dependence of magnetization in MnV_2O_4 single crystal. (b) Temperature dependence of the (400) and (200) Bragg peaks integrated intensities showing the existence of two magnetic transitions. The solid lines are guides to the eye. (c) Splitting of the (400) cubic peak into two tetragonal peaks $(220)_T$ and $(004)_T$.

the 3-axis spectrometer TASP, at the SINQ spallation source. For these, we made use of a single crystal of about 1.3 g, aligned in the (hhl) horizontal scattering plane. Elastic measurements were carried out using a monochromatic neutron beam ($\lambda = 3.19$ Å) and $20'$ collimators in front and after the sample. For the inelastic neutron scattering (INS) measurements, TASP spectrometer was operated with a fixed final energy $E_f = 3.5$ meV, open $-$ $40' - 40' - 80'$ collimation, and a cooled Be filter after the sample.

Figure 1(b) shows the evolution with temperature of the (400) and (200) peaks integrated intensities, measured using the SCD. Diffraction peaks are indexed in the cubic-spinel structure. The (400) peak starts to increase at approximately 60 K (T_F) and exhibits a kink at about 52 K (T_S). As the temperature is lowered, the intensity continues to increase and saturates below 45 K. It is noteworthy that the order-parameter profile shows a long tail which extends above 70 K. This may be due to the critical scattering associated with a short-range order above T_F. A very similar temperature dependence was observed for the (220) peak, measured using the 3-axis spectrometer [Fig. 3(b)]. In contrast, the (200) reflection, which is forbidden in the cubic symmetry ($Fd\bar{3}m$), appears only below T_S and increases as the temperature decreases. Further examination of diffraction data confirmed that the transition at T_S is related to the modification of the crystal structure. The occurrence of tetragonal distortion is clearly demonstrated in the Fig. 1(c) by the splitting of the (400) Bragg peak into two components, indexed as $(220)_T$ and $(400)_T$ in the tetragonal cell ($a_T \approx a/\sqrt{2}$ and $c_T \approx c$).

The low-temperature crystal structure was determined from a complete set of SCD data that mapped the entire reciprocal space. Mixed nuclear and magnetic reflections with Q $(= 4\pi \sin\theta/\lambda) \leq 7$ Å^{-1} were excluded from the structure refinement, carried out using GSAS [14]. The systematic absences among high-Q reflections confirmed the $I4_1/a$ space group, proposed in Ref. [12]. This space group implies a relaxation of the symmetry constraints at the oxygen positions. The compression of the VO_6 octahedra along the c axis ($c_T/a_T \approx 0.98$) is accompanied by a small distortion of the V–O bonds in the basal plane. Referring to Fig. 2(a) which displays the V-tetrahedron along the c axis, the V–O bonds are arranged in an antiferrodistortive alternating pattern with short (dashed lines) and long (bold lines) distances. This is consistent with the so-called A-type orbital ordering with antiferro-order along the c axis and ferro- in the ab plane, similar to that proposed by Tsunetsugu and Motome [4,5] for V spinels with nonmagnetic A-site cations.

Between the two transition temperatures (T_F, T_S), the magnetic scattering appears only on top of the structural reflections, as expected for a ferrimagnetic ordering. Below T_S, one observes the appearance of additional magnetic peaks $(hk0)$ with h, $k \neq 2n$, forbidden in the $I4_1/a$ symmetry. For instance, the cubic (200) reflection, indexed

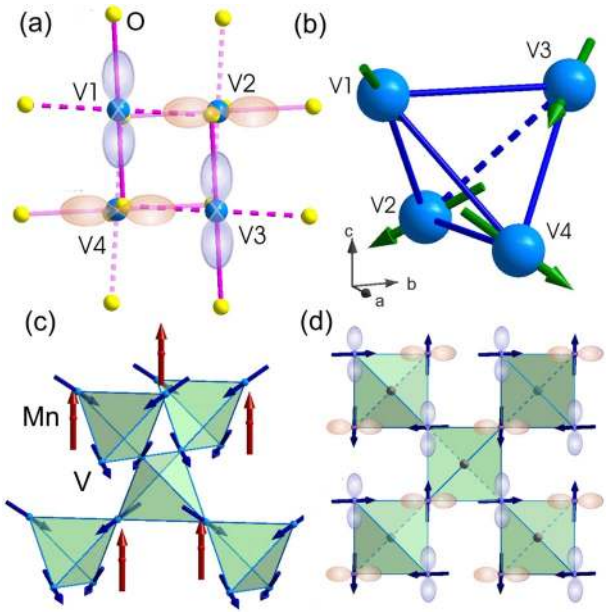

FIG. 2 (color online). (a) Projection of the V_4 tetrahedron in the ab plane. V–O bonds are arranged in an alternating pattern giving rise to a staggeredlike orbital ordering. (b), (c) Graphical representations of the low-temperature noncollinear ferrimagnetic structure of the MnV_2O_4. The Mn moments are aligned parallel to the c axis, while the V moments are canted by approximately 65°. (d) Projection of the magnetic structure on the basal plane.

in the tetragonal phase as $(110)_T$, is purely magnetic and can be explained by an antiferromagnetic (AFM) arrangement within the ab plane. Nevertheless, the c-axis components of Mn and V moments remain ferrimagnetically ordered. To generate all the spin configurations compatible with the crystal symmetry we carried out a group theory analysis [15] using the program SARAh [16]. There are eight irreducible representations (IR) associated with the $I4_1/a$ space group and $k = (0, 0, 0)$. Among these, only one allows for a ferrimagnetic alignment of Mn and V sublattices. The basis vectors of this representation are listed in Table I. It shows that the Mn moments are aligned parallel to the tetragonal c axis, while the V moments can have components on any of the three crystal axes. The a and b-axis components are constrained to form an orthogonally stacked AFM structure as shown in Fig. 2. This shows the inadequacy of the model previously proposed by Plumier [10] with V moments lying in (h00) sheets.

Full refinements of various symmetry-allowed magnetic structure models were performed using high-resolution powder diffraction data. The use of powder sample avoids complications related to magnetic domains and extinctions. Rietveld refinements were performed using the FULLPROF program [17]. Above the structural transition, the diffraction pattern was fitted using a collinear ferrimagnetic model, with the Mn and V moments aligned antiparallel to each other. Such a collinear order may be stabilized by an order-by-disorder mechanism [18], as previously suggested in Ref. [5]. As discussed above, below T_S the V moments develop AFM components in the ab plane. As the Mn moments produce a strong effective magnetic field for the V ions, the V moments tend to orient themselves almost perpendicular to it. The magnetic structure model shown in Table I gave the best fit to the diffraction pattern. Refinements using spherical Mn^{2+} and V^{3+} form factors, on the 5 K data, yielded the ordered moments: $m_{\mathrm{Mn}} \approx 4.2\mu_B$ and $m_{\mathrm{V}} \approx 1.3\mu_B$. The V moments are canted with respect to the c axis by approximately 65.12°. A stereographic view of the magnetic structure is displayed in Fig. 2(b) and 2(c). The ab projections of V moments are antiparallel within each layer and orthogonal between layers. According to the Kugel-Khomskii prediction [19], this arrangement may favor the A-type orbital order. The compatibility between the magnetic and a staggered orbital ordering is illustrated in Fig. 2(d).

TABLE I. Basis vectors (BVs) of an IR of the space group $I4_1/a$ and $k = (0, 0, 0)$. BVs are defined relative to the tetragonal axes. Magnetic moments for an atom j is given by $m_j = \sum_i C_i\psi_i$, where C_i is the mixing coefficient of BVs ψ_i.

	ψ_1		
Mn1 $(0, \frac{1}{4}, \frac{1}{8})$	(0 0 1)		
Mn2 $(\frac{1}{2}, \frac{1}{4}, \frac{3}{8})$	(0 0 1)		
	ψ'_1	ψ'_2	ψ'_3
V1 $(0, 0, \frac{1}{2})$	(0 0 −1)	(1 0 0)	(0 1 0)
V2 $(\frac{1}{4}, \frac{3}{4}, \frac{1}{4})$	(0 0 −1)	(0 1 0)	(−1 0 0)
V3 $(0, \frac{1}{2}, \frac{1}{2})$	(0 0 −1)	(−1 0 0)	0 −1 0)
V4 $(\frac{3}{4}, \frac{3}{4}, \frac{1}{4})$	(0 0 −1)	(0 −1 0)	(1 0 0)

The structural investigation was complemented with inelastic neutron scattering measurements performed at different temperatures ranging from 1.5 K to 70 K. The spin-wave spectrum across the Brillouin zone was measured in a series of constant-Q scans. At 1.5 K, the spectrum consists of a gapped acoustic mode (with the gap of about 1.5 meV) and several optical branches. The dispersion of the low-energy mode along the c axis is shown in the inset of Fig. 3(a). A detailed analysis of the spectrum will be reported elsewhere [20]. Here we will focus only on the temperature behavior of the energy gap. Figure 3(a) shows the energy scans measured at the zone center (220) at various temperatures. Fits of the gap mode, indicated by solid lines in Fig. 3(a), were done using a cross-section function:

$$\frac{d^2\sigma}{d\Omega dE'} \propto \frac{\mathbf{A_q}}{\omega_{\mathbf{q}}}\mathbf{L}(\omega - \omega_{\mathbf{q}}, \Gamma)[n(\omega_{\mathbf{q}}) + 1], \qquad (1)$$

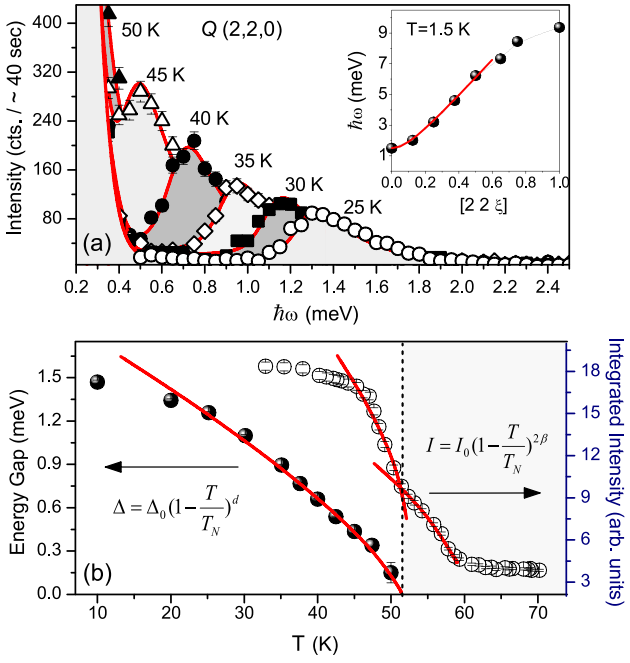

FIG. 3 (color online). (a) Energy scans measured at different temperatures, at $Q = (2\ 2\ 0)$. Solid lines are fits to the data as described in the text. Inset: dispersion of the low-energy spin-wave branch along the c axis, measured at 1.5 K. (b) Variation with the temperature of the energy gap (●) and (220) peak intensity (○). The gap mode extrapolates to zero at the structural transition temperature. The solid lines are power-law fits.

where $\mathbf{A_q}$ term describes the q dependence of the intensity, $\mathbf{L}$ is a Lorentzian peak-shape function of width Γ, and $[n(\omega_\mathbf{q}) + 1]$ is the Bose factor. The approximate dispersion relation near the zone center was written as $\omega_\mathbf{q}^2 = \Delta^2 + (v\mathbf{q})^2$, where v is the spin-wave velocity determined to be approximately 1.88 meV. The model cross section was numerically convoluted with the spectrometer resolution function [21].

The variation of the energy gap, Δ, with temperature is shown in Fig. 3(b). It decreases with increasing temperature and vanishes, moving into the incoherent peak, exactly at the structural transition (T_S). To quantify the temperature dependence of the gap, we performed a least-square fit using the power law $\Delta(T) \propto (T_S - T)^d$. The fit yielded an exponent $d \simeq 0.73(2)$. For comparison, Fig. 3(b) displays the temperature dependence of the (220) Bragg peak intensity, measured simultaneously with the inelastic data. Near the two phase transitions, the variation with temperature of the order parameter was described as $I(T) \propto (T_{F,S} - T)^{2\beta}$. The critical exponents are $\beta_1 \simeq 0.32(4)$ at the first transition, and $\beta_2 \simeq 0.34(5)$ for the second. Although the fits were done over a limited number of data points, one should point out that the obtained values are close to those of the 3D Heisenberg ($\beta = 0.36$) or 3D Ising ($\beta = 0.33$) models. Comparing these exponents with that measured for $\Delta(T)$ shows that the energy of the gap mode varies roughly as the square of staggered magnetization. The energy gap in the spin-wave spectrum can be explained by the existence of single-ion anisotropy. Such anisotropy may be a consequence of the unquenched orbital angular momentum of the V^{3+} ion.

In summary, our neutron scattering measurements on MnV_2O_4 show the existence of two consecutive magnetic transitions. The first transition is from a paramagnetic to collinear ferrimagnetic state. At a slightly lower temperature the ferrimagnetic state becomes noncollinear, with V spins developing AFM components in the ab plane. There is a simultaneously structural distortion to an orbitally ordered tetragonal phase. The appearance of an anisotropy gap indicates a strong influence of the V orbital angular momentum. A proper theory for spin and orbital physics in MnV_2O_4 should account for these observations.

The authors thank D. Abernathy, O. Tchernyshyov, and M. Whangbo for valuable discussions and interest in this work. Work at ORNL was supported by the US Department of Energy (DOE) under Contract No. DE-AC05-00OR22725 with UT-Battelle, LLC. Work at ANL was supported by the US DOE, Office of Science, Office of Basic Energy Sciences, under Contract No. DE-AC02-06CH11357. We also acknowledge the support of the NIST, US Department of Commerce, in providing the neutron research facilities used in this work.

*garleao@ornl.gov

[1] H. Mamiya, M. Onoda, T. Furubayashi, J. Tang, and I. Nakatani, J. Appl. Phys. **81**, 5289 (1997).
[2] Y. Ueda, N. Fujiwara, and H. Yasuoka, J. Phys. Soc. Jpn. **66**, 778 (1997).
[3] N. Nishiguchi and M. Onoda, J. Phys. Condens. Matter **14**, L551 (2002).
[4] H. Tsunetsugu and Y. Motome, Phys. Rev. B **68**, 060405(R) (2003).
[5] Y. Motome and H. Tsunetsugu, Prog. Theor. Phys. Suppl. **160**, 203 (2005).
[6] Y. Motome and H. Tsunetsugu, J. Phys. Soc. Jpn. Suppl. **74**, 208 (2005).
[7] O. Tchernyshyov, Phys. Rev. Lett. **93**, 157206 (2004).
[8] S. Di Matteo, G. Jackeli, and N. B. Perkins, Phys. Rev. B **72**, 020408(R) (2005).
[9] T. Maitra and R. Valentí, Phys. Rev. Lett. **99**, 126401 (2007).
[10] R. Plumier and M. Sougi, Solid State Commun. **64**, 53 (1987); Physica (Amsterdam) **155B**, 315 (1989).
[11] K. Adachi, T. Suzuki, K. Kato, K. Osaka, M. Takata, and T. Katsufuji, Phys. Rev. Lett. **95**, 197202 (2005).
[12] T. Suzuki, M. Katsumura, K. Taniguchi, T. Arima, and T. Katsufuji Phys. Rev. Lett. **98**, 127203 (2007).
[13] S.-H. Baek, K.-Y. Choi, A. P. Reyes, P. L. Kuhns, N. J. Curro, V. Ramanchandran, N. S. Dalal, H. D. Zhou, and C. R. Wibe, arXiv:0707.0018v1.
[14] A. C. Larson and R. B. Von Dreele, General Structure Analysis System (GSAS), Los Alamos National Laboratory Report LAUR, 86–748, 1994.
[15] O. V. Kovalev, in *Representations of the Crystallographic Space Groups*, edited by H. T. Sokes and D. M. Hatch (Gordon and Breach, New York, 1993).
[16] A. Wills, Physica (Amsterdam) **276B**, 680 (2000); program available from www.ccp14.ac.uk.
[17] J. Rodriguez-Carvajal, Physica (Amsterdam) **192B**, 55 (1993); program available at www.ill.fr/dif/Soft/fp/.
[18] J. Villain, J. Phys. C **10**, 1717 (1977).
[19] K. I. Kugel and D. I. Khomskii, Zh. Eksp. Teor. Fiz. **64**, 1429 (1973) [Sov. Phys. JETP **37**, 725 (1973)].
[20] V. O. Garlea *et al.* (unpublished).
[21] M. Popovici, Acta Crystallogr. Sect. A **31**, 507 (1975).